This is a repository copy of *In Situ Scanning Transmission Electron Microscopy of Ni Nanoparticle Redispersion via the Reduction of Hollow NiO*.

White Rose Research Online URL for this paper:
https://eprints.whiterose.ac.uk/126787/

Version: Accepted Version

Article:

In-Situ Scanning Transmission Electron Microscopy of the Reduction of Hollow NiO Nanostructures for Catalyst Regeneration

Alec P. LaGrow,[†,‡,*] David C. Lloyd,[†,‡] Pratibha L. Gai[†,‡,δ*] and Edward D. Boyes,[†,‡,§*]

The York Nanocentre,[†] Department of Physics,[‡] Electronics,[§] and Chemistry,[δ] University of York, York, YO10 5DD, U.K.

ABSTRACT: Oxidation and reduction cycles are used in the regeneration of nanoparticle catalysts that have deactivated due to sintering and poisoning. We examine the case of nickel oxidation and reduction on the regeneration of the smallest end of the particle size distribution via *in-situ* high angle annular dark field environmental scanning transmission electron microscopy (HAADF-ESTEM). Cycling the Ni/NiO system through successive redox cycles shows that the particles retain the same general size distributions even though Ostwald ripening and particle migration and coalescence is occurring. The regeneration of the smallest nanoparticle sizes which disappear due to sintering processes occurs by the ejection of small (2-3 nm) nickel particles during the reduction of the hollow nickel oxide nanostructures. The nickel nanoparticles above ~3.5 nm in size, form hollow polycrystalline nickel oxide upon oxidation. Upon reduction, the grains making up the shell of the hollow nickel oxide reduce separately at the grains surface and at the grain boundaries between the polycrystalline grains. The contraction in particle size upon reduction destabilizes the hollow nanostructure and causes the particle to rearrange and collapse. As this process occurs, some parts of the particle are ejected from the reducing particle and form small particles of nickel, which regenerate the smallest parts of the size distribution. Once the particle collapses, the nickel rearranges reforming solid nickel nanoparticles enclosed by their low index facets.

Nanoparticle catalysts have been shown to have numerous advantages over their bulk counterparts due to their high surface to volume ratios and size dependent properties.[1] The major limitations for industrial nanoparticle catalysts are deactivation mechanisms, such as sintering, which leads to increases in particle size and loss of crystal facets.[2] One of the main mechanisms that causes loss of catalytic efficiency is Ostwald ripening, where larger particles grow at the expense of smaller particles via atom migration.[2-4] The other main mechanism is particle migration and coalescence.[2] Several methods have been employed to try and limit Ostwald ripening, including tailoring the particle support interaction[5] and minimizing the size distribution of the initial nanoparticle sample.[6] Additionally particle regeneration can be employed through particle redispersion to regenerate highly active nanoparticles with small particle sizes.[7-9] One method that has proven promising is using oxidation and reduction cycles to re-disperse the nanoparticles and form small catalytically active particles.[9-12] Oxidation and reduction cycles can also be used to regenerate poisoned catalysts by oxidizing the poisoning agent, such as removing sulfidation in nickel catalysts.[13]

However, the mechanisms of regeneration are still poorly understood as detailed mechanistic data on nanoparticle oxidation and reduction is limited. One method that is increasingly utilized for studying how nanoparticle catalysts behave under simulated reaction conditions is *in-situ* electron microscopy. *In-situ* electron microscopy studies of nanoparticles under reaction conditions was pioneered with the development of the atomic resolution environmental transmission electron microscope (ETEM)[14] and specialised sample stages that allow for heating in gas environments.[15-18] Early work showed how the loss of catalytic activity occurred due to Ostwald ripening and particle migration and coalescence of nanoparticles, and the speed of these processes was influenced by the temperature[19-21] and the gas environment.[4, 21-23] *In-situ* studies have also shown that the exposed facets of the nanocrystals are modified by the reaction conditions and gases used.[24-26] Recently high angle annular dark field environmental scanning transmission electron microscopy (HAADF-ESTEM) was implemented to study oxidation and reduction through the changes in the density of the material (Z-contrast) during oxidation.[27]
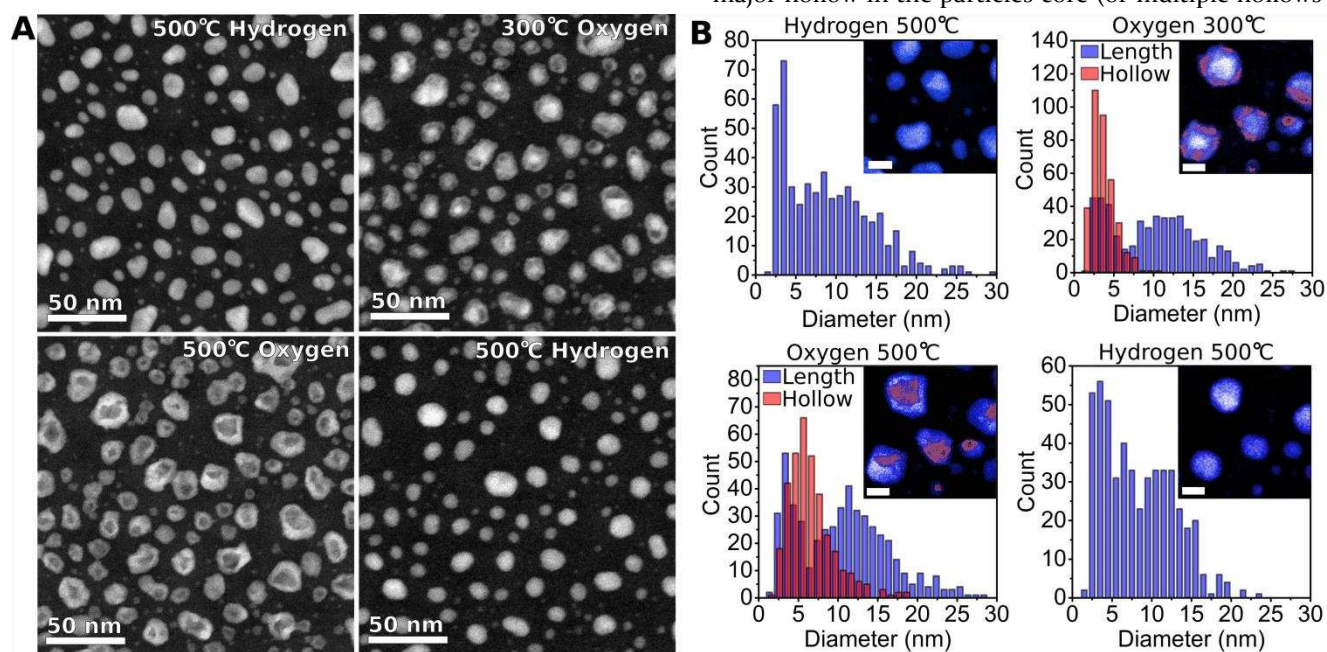
Of particular interest are highly catalytic and chemically reactive systems such as nickel. Due to the materials susceptibility to oxidation it has been shown that a native oxide layerwill be present in synthesized nanoparticles[28-29] and further oxidation occurs at elevated temperatures.[30-31] Furthermore, full oxidation of nickel nanoparticles occurs via differential diffusion and leads to hollowing of the nanoparticles and the formation of polycrystalline hollow nickel oxide.[32] Tracy *et al.* have shown that Ni nanoparticles from 9 – 96 nm in size undergo hollowing in the formation of the NiO nanostructures which then could be reduced back to similar sized solid Ni nanoparticles.[33-34] Under reaction conditions, such as for the Steam refor-

mation reaction, Ni nanoparticles were observed to rapidly undergo Ostwald ripening, where the largest nanoparticles grew at the expense of the smallest.[30]

We study the oxidation of Ni nanoparticles to hollow NiO and their reduction to solid Ni nanoparticles via ESTEM, showing their sintering and regeneration during these cycles. Oxygen and hydrogen environments promote sintering mechanisms such as Ostwald ripening and particle migration and coalescence, while the oxidation and reduction cycles cause the regeneration of the nanoparticles and the formation of small solid Ni particles during the reduction of the hollow NiO nanostructures. The reduction mechanism is studied in detail elucidating how the reduction mechanism occurs at the surface of the grains and the grain boundaries making up the polycrystalline hollow NiO nanostructures.

EXPERIMENTAL METHODS

The model samples were all prepared by magnetron sputtering nickel nanoparticles from a nickel target (99.95% from Testbourne Ltd) using a JEOL JFC-2300HR fine-coater by sputtering 0.7 nm Ni at 80 mA. The nanoparticles were deposited onto an amorphous SiN$_x$ membrane supported by a Wildfire MEMS chip made by DENS Solutions for *in-situ* heating. The initial sputtered Ni nanoparticles were then reduced at 500 °C in hydrogen before experiments were carried out to generate oxide free nickel.[27] This was considered to be the starting point of the experiments.

fied in-house by Boyes and Gai,[35-36] operating at 200 kV. The temperature was controlled with a MEMS heating stage from DENS Solutions. For the *in-situ* studies, the gas was introduced into the ESTEM with a pressure of 2 Pa at the sample. For the oxidation, oxygen gas (99.999% from BOC UK) was used. For the reduction, hydrogen gas (99.9995% from BOC UK) was used. The images were 1024×1024, with a pixel dwell time of 19.5 µs. The particles were only exposed to the electron beam during data setup and acquisition. To minimize beam effects, calibration procedures were employed,[27, 36] and the images were compared to oxidation and reduction series carried out without exposing the particles to the beam.
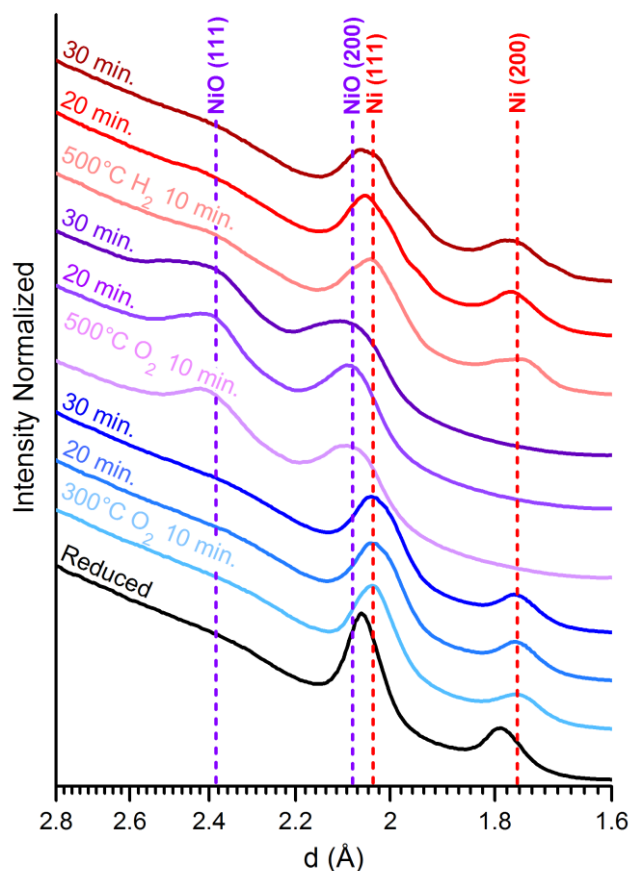
RESULTS AND DISCUSSION

A single cycle of oxidation and reduction of the nickel was studied, starting with Ni metal, then creating hollow NiO and regenerating the Ni metal. The same area of nanoparticles was imaged once every 30 minutes. The initial nanoparticles formed after the hydrogen reduction at 500 °C for 30 minutes were Ni nanoparticles with a size distribution of 9 ± 6 nm in diameter (**Figure 1 A** and **B**). Upon introduction of oxygen at 300 °C for 30 minutes the nanoparticles increased in size to 10 ± 6 nm. The particles had an oxide shell of 2.8 ± 0.7 nm, with voids of 3.6 ± 1.5 nm occurring between the nickel core and the nickel oxide shell. After the particles were exposed to oxygen at 500 °C for 30 minutes the nanoparticles increased in size to 11 ± 6 nm. This was accompanied by the formation of a single major hollow in the particles core (or multiple hollows in

Figure 1. *In-situ* HAADF-ESTEM images of a single area of nanoparticles after 30 minutes at 500 °C in hydrogen, 300 °C in oxygen, 500 °C in oxygen, and 500 °C in hydrogen. **B)** Size distributions of the same area show the particle size in blue and the size of the hollows in red. The insets of **B)** show a zoom in of an area in **A)** with the particles coloured blue and the hollows coloured in red.

The *in-situ* analysis was carried out on a double aberration-corrected Environmental (Scanning) Transmission Electron Microscope (AC-E(S)TEM) JEOL 2200FS modi-

the biggest particles) of 6.5 ± 2.9 nm (Figure 1 B). The shell thickness of the particles increased to 4.6 ± 1.3 nm. Hollowing was witnessed in most particles and was no

longer seen below 3.5 nm in size with the smallest particles, 4 ± 2 nm, being solid (**Figure S1**). During oxidation the hollowing was witnessed to occur from the formation of surface voids or a single void from one side of the particle at 300°C, which became a single central hollow at 500°C. Upon reduction, the particles were roughly spherical Ni with an average size of 8 ± 4 nm.
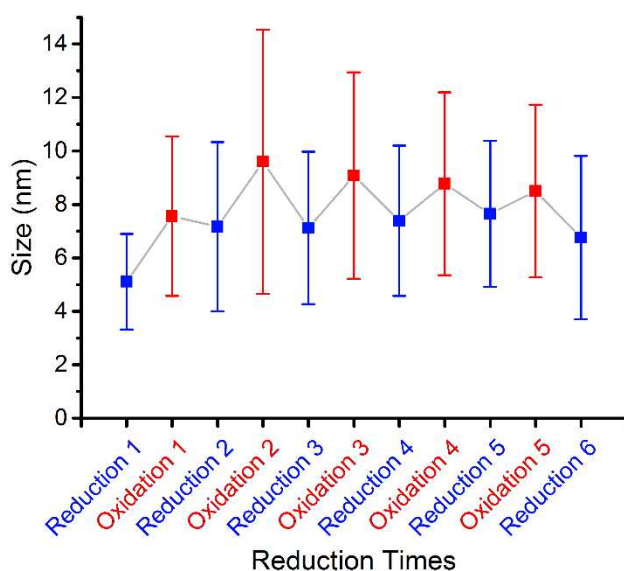
During the oxidation of the nanoparticles it can be seen that certain particles oxide layers fuse with nearest neighbours (**Figure 1** and **Figure S2**). When the nanoparticles are reduced the fused nanoparticles do not separate and form a single particle (**Figure 1** and **Figure S2**). Particles are also seen to migrate together and fuse during reduction (**Figure S3**). At the same time the particles that are reformed are more symmetrical then the initially formed Ni nanoparticles leading to a reduction of the largest diameters in the tail of the size distribution. These processes would occur in multiple ways. During the oxidation and reduction, significant rearrangement is observed to occur as well as fusion of particles which would lead the particles to adopt their low energy configurations, as well as to reduce the number of particles present. Ostwald ripening was observed to be occurring while the particles were in a hydrogen atmosphere at these temperatures (**Figure S4**).

The particles were reduced initially in hydrogen forming *fcc* Ni, as shown by the electron diffraction (**Figure 2**). Oxygen was introduced at 300°C. Oxidation is evident in STEM[27] with thin oxide shells and voids between the shell and the core. The diffraction, however, shows the particles are still predominantly Ni at 300°C under oxygen, indicating that the cores are still nickel and are dominating the diffraction signal. At 500°C in oxygen the particles quickly oxidize to NiO, as they fully hollow out. Once the hydrogen is re-introduced, the nanoparticles were reduced to Ni metal, with the nickel signal dominating within 10 minutes of the hydrogen being introduced at 500°C.

To understand the redox cycling of the Ni nanoparticles the experiment was repeated with a Ni sample of a smaller size distribution of 5 ± 2 nm. The reduction and oxidation was carried out 6 times, each for 30 minutes in hydrogen or oxygen. The initial size distribution of the nanoparticles was observed to increase from the first to the second cycle of reduction (5 ± 2 nm to 7 ± 3 nm) and oxidation (8 ± 3 nm to 10 ± 5 nm); and then the particles size plateaued (**Figure 3**). For the case of the reduced particles after the initial oxidation and reduction the size and size distribution remained constant, ending at 7 ± 3 nm in size after 6 cycles. For the oxidized particles the size distribution was observed to decrease over the cycles, finishing at 9 ± 3 nm (**Figure 3**).

Figure 2. Time resolved radially averaged *in-situ* electron diffraction during the reaction, at 10 minute intervals. The (111) and (200) peaks of NiO are shown in purple, and the (111) and (200) peak of Ni in red.

Figure 3. Nanoparticle size distributions showing their average size (square) and standard deviations of their size (error bars) across multiple reduction and oxidation experiments of a single sample.

During the redox reactions, the particles are seen in two distinct forms, solid Ni nanoparticles enclosed by low index facets, and hollow NiO nanoparticles. The hollow NiO contains obvious grain boundaries between the different grains in the polycrystalline shell (white arrows in **Figure 4 A**). After reduction of the nanoparticles, the sol-

id Ni particles are bound by their low index facets (**Figure 4 B** and the FFT inset). The regenerated particles can be reformed as single crystals (**Figure 4 B**), indicating a large degree of rearrangement accompanying the reduction.
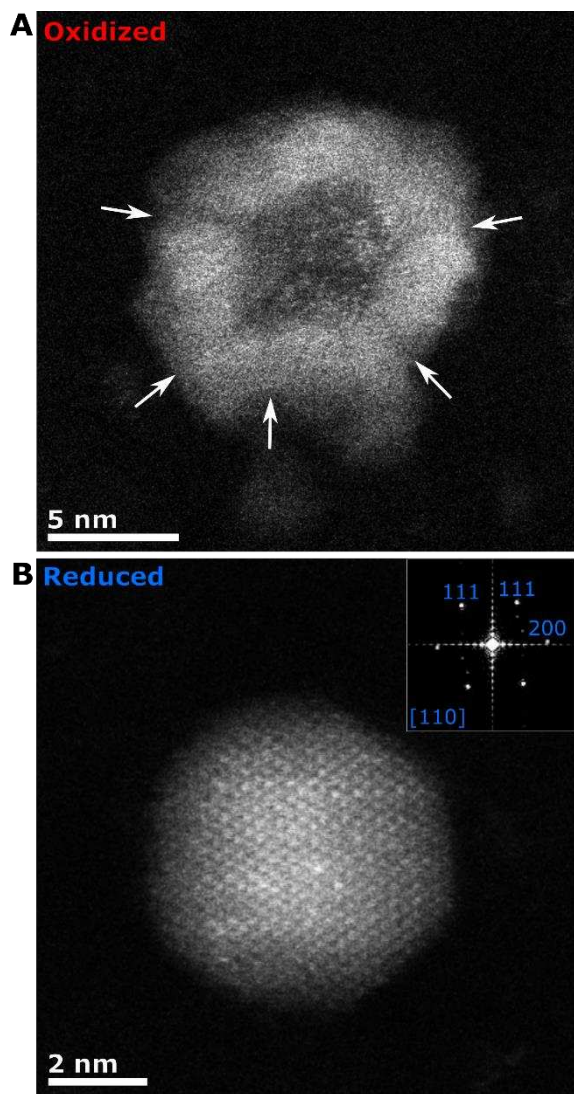
Figure 4. High resolution HAADF-ESTEM images of **A)** hollow NiO nanoparticle and **B)** a solid Ni nanoparticle after reduction again. The white arrows indicate some of the grain boundaries in the hollow NiO. The inset of the FFT in **B)** indicates that the particle is viewed down the [110] zone axis and enclosed by low index facets.

To study how the reduction occurs, the same area was followed during the reduction process (**Figure 5**). It is interesting to note that the reduction occurs at different rates based on the individual particles. For particle 4 the reduction occurs by the time the temperature reaches 500°C. The other particles reduce after reaching 500°C with particle 1 taking ~5 minutes after being elevated to 500°C, particle 2 taking ~13 minutes and particle 3 taking ~7.5 minutes. The difference in the reduction rate cannot be explained by particle size as although particle 4 which is the smallest is reduced the fastest, the second fastest is

particle 1 which is the largest. It is more relevant to look at the reduction in terms of the size of the grains and the density of grain boundaries making up the polycrystalline hollow NiO nanoparticle. Once the domains start to reduce, the particles rapidly rearrange to form a single Ni nanoparticle. The period between onset of noticeable rearrangement to form Ni nanoparticles ranged from under 1 minute for particle 4, to 13 minutes for particle 2. When the reduction was carried out at 400°C for 30 minutes, reduction was seen to occur; but only with a fraction of the particles, and once the temperature was increased to 500°C the rest of the particles were completely reduced (**Figure S5**). Images taken where the reflections of NiO and Ni are observable shows that the initial structure is NiO, and the final structure is Ni (**Figure S6**)
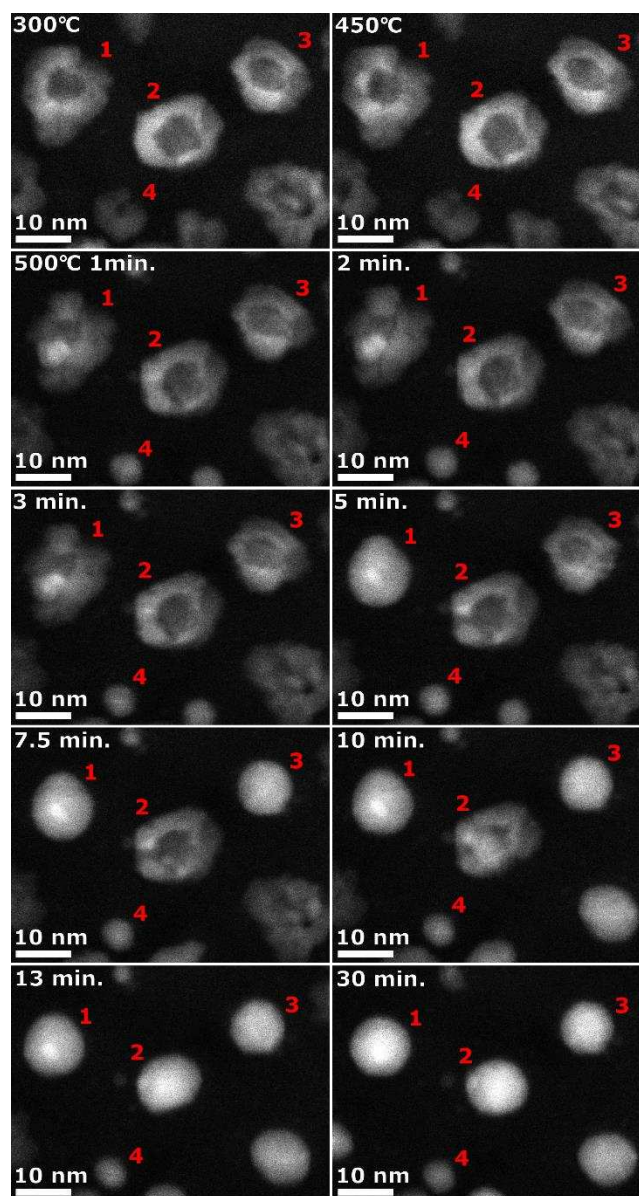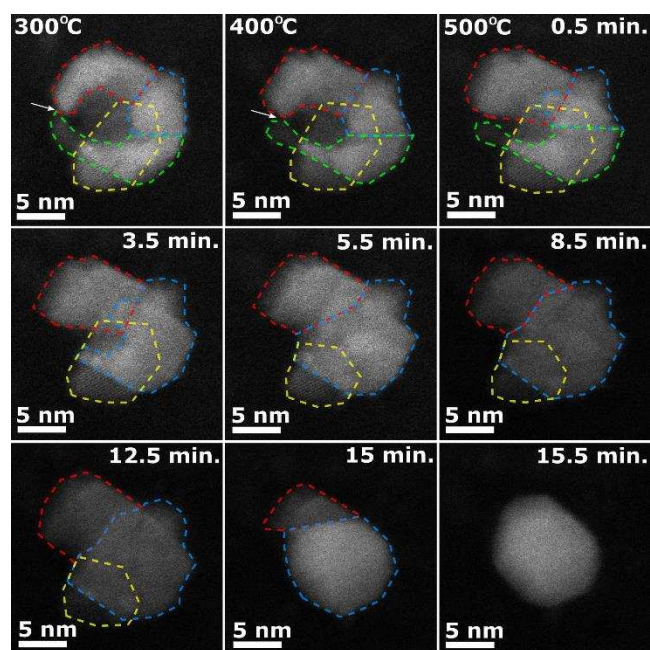

Figure 5. HAADF-ESTEM images of the *in-situ* reduction of hollow NiO nanoparticles in 2 Pa hydrogen starting at 300°C and then occurring at 500°C for 30 minutes. Individual particles are numbered in red.

To study the intensity changes during reduction, particle 2 was magnified and the images were colorized (**Figure 6**). The particle was chosen as obvious changes in the intensity in the shell occurs during reduction. These changes in intensity would be due to the formation of a Ni rich or pure Ni phase and the start of the oxide reduction. At 300°C in hydrogen no change is seen from the as oxidised sample, by 470 °C the centre of the grain boundary has lost its intensity (shown by the white arrow). The intensity at the grain boundaries continues to drop as the NiO grains contract (1 to 7.5 minutes, white arrows) and intensity builds up next to the grain boundary (3 to 7.5 minutes, white intensity in the thermal colour scheme). These bright regions occur at the edges of the disappearing grain boundaries in the hollow NiO particle, and indicate that the Ni atoms nucleate near the edge of the grain boundaries in the NiO where the reduction occurs. As the grains reduce, they shrink causing the shell to become unstable. The reduced grains then coalesce at the local center of mass (shown by black arrows in **Figure 6**, 7.5 minutes and 10 minutes). Finally, the particle rearranges to form a central roughly spherical nanoparticle. After 13 minutes the reduction has occurred fully. It is observed that as the particles reform, smaller nanoparticles are ejected from the reducing shell forming particles of 3 nm and of 2 nm, around the parent particle (as shown by the red arrows).
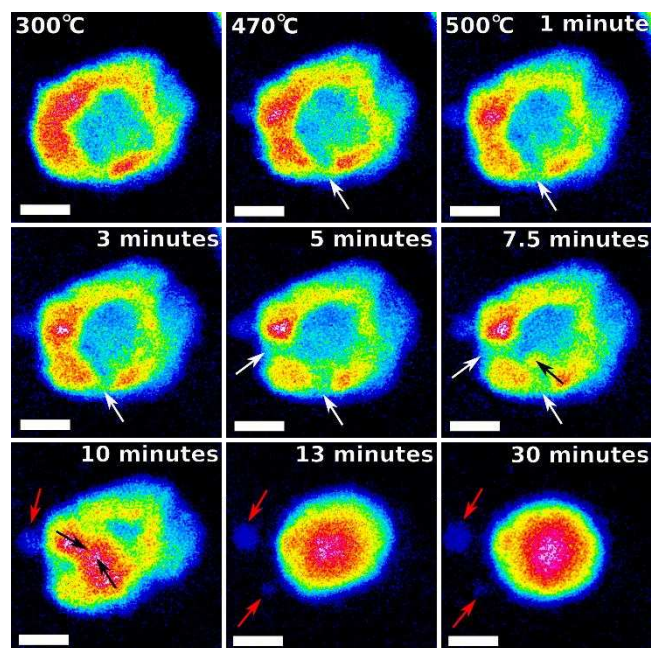
Figure 6. *In-situ* HAADF-ESTEM images of the reduction of a single particle of NiO in 2 Pa hydrogen, with thermal colours applied to show the changes in intensity with time more clearly. White arrows point out where breaks occur in the shell of the nanoparticle, and the red arrows point out small particles that break away from the nanoparticle and the black arrows show the movement of the grains during the reduction. All scale bars are 5 nm.

The initial NiO structures are shown to be polycrystalline with the individual grains of NiO outlined by dashed red, green, blue and yellow lines (**Figure 7**). As the reduction proceeds, the initial reduction occurs at the grain boundaries with the contraction of the reducing NiO causing the grain boundary to open completely by 0.5 minutes at 500°C (**Figure 7**, white arrow). After this the individual grains (as noted by the dashed lines) shrink and rearrange separately. First the grain boundary breaks and the green grain reduces in size until it becomes indistinguishable from the blue grain by 3.5 minutes. Then the yellow grain is seen to shrink, and then merge with the blue grain by 15 minutes. The red grain shrinks until by 15 minutes there is a solid nickel grain denoted by the blue lines with a mostly reduced grain denoted by the red lines. These two grains are still separated by the initial crystallographic grain boundary that was seen in the polycrystalline NiO shell at 300°C (as shown by the red and blue dashed lines). By 15.5 minutes the red grain rearranges and fuses with the larger blue grain to form a single faceted particle of Ni. It should be noted, as the hollow NiO is a 3-dimensional structure, additional grains that are not directly observed would also be present and rearranging.

Figure 7. High resolution *in-situ* HAADF-ESTEM images of the reduction of a single particle of NiO in 2 Pa hydrogen. The guides in yellow, green, blue and red define individual grains in the polycrystalline shell/ major areas in the reduction process. The white arrow points to a grain boundary that opens during the reduction.

In this redox study we show that the particle size of the Ni and NiO nanoparticles remain relatively constant even though sintering occurs during oxidation and reduction. The oxidation occurs by differential diffusion where the diffusion rate of the nickel is much greater then the diffusion of the oxygen.[32, 34] The oxidation starts by forming

surface voids as the faster diffusing Ni diffuses outwards and the NiO causes a large lattice expansion of the crystal structure. The expansion causes defect formation, the formation of voids, and the formation of separate grains of NiO.[37-38] The vacancies, formed from the outward diffusion of the Ni cations and the lattice expansion caused by the oxidation, diffuses inwards and coalesce to form a single hollow.[37] The regeneration of the average particle size occurs as small particles are formed during reduction. The reduction occurs at the domain interfaces in the polycrystalline shell, with the nucleation of Ni atoms at the grain boundary. As the reduction proceeds there is a loss in nanoparticle size due to the ~17% contraction in lattice parameter, destabilizing the shell structure. As the particle domains contract, the shell becomes structurally unstable due to its three-dimensional nature and collapses. This unstable shell gives rise to the formation of the smallest sizes of Ni nanoparticles, which are ejected during collapse of the hollow NiO. At 500°C, the particles have enough energy to rearrange and remove defect structures that form from reducing a polycrystalline shell structure. In this way, low energy faceted nickel nanoparticles are reformed.

Particle disintegration upon reduction is common,[39] as there is a large difference in lattice parameter between the oxidized and reduced species.[40] The reduction of hollow oxide nanoparticles has been observed previously to regenerate cobalt catalysts.[10] Particle rearrangement and reformation occurs during the experiment, and indicates that the reduced Ni° atoms are mobile on the particles surface at these temperatures (500°C), allowing them to rearrange and reform spherical faceted Ni particles. This is consistent with previous studies reporting high Ni° mobility.[41]

The different rates of reduction and particle collapse observed in this study are in-line with previous studies that show an induction period before reduction begins, and then an autocatalytic reaction occurs where the reduction rate increases as the size of the nickel cluster increases.[41-43] The induction period has also been postulated to occur due to the slow initial generation of O vacancies in the NiO structure, creating a more reactive surface for hydrogen splitting.[44] This could explain the different reduction speeds as the different NiO particles would have different densities of defects in their structure, leading to a different number of oxygen vacancies.

CONCLUSIONS

We have shown the recyclability of nickel nanoparticles and the renewal of their size distributions based upon the reduction mechanism of hollow NiO nanoparticles to solid Ni nanoparticles. The NiO is observed to reduce from the grain boundaries between the polycrystalline grains, until the structure becomes unstable and rapidly collapses and fuses together to form single solid particles. The reduction of the NiO is seen to occur at different rates and start at different times over the course of approximately 30 minutes at 500 °C under 2 Pa hydrogen. The difference in the reduction times is in line with litera-ture reports of NiO having an induction period followed by autocatalytic reduction. During the reduction, some of the NiO domains release small amounts of Ni, which leads to the regeneration of the smaller particle sizes which are seen to be consumed during the redox cycles by Ostwald ripening and particle fusion.

AUTHOR INFORMATION

Corresponding Author

*alec.lagrow@york.ac.uk; *pratibha.gai@york.ac.uk; *ed.boyes@york.ac.uk

Author Contributions

The manuscript was written through contributions of all the authors.

REFERENCES

(1) Zaera, F., Nanostructured materials for applications in heterogeneous catalysis. *Chemical Society Reviews* **2013,** *42*, 2746-2762.

(2) Hansen, T. W.; DeLaRiva, A. T.; Challa, S. R.; Datye, A. K., Sintering of Catalytic Nanoparticles: Particle Migration or Ostwald Ripening? *Acc. Chem. Res.* **2013,** *46*, 1720-1730.

(3) Martin, T. E.; Gai, P. L.; Boyes, E. D., Dynamic Imaging of Ostwald Ripening by Environmental Scanning Transmission Electron Microscopy. *Chemcatchem* **2015,** *7*, 3705-3711.

(4) Simonsen, S. B.; Chorkendorff, I.; Dahl, S.; Skoglundh, M.; Sehested, J.; Helveg, S., Direct Observations of Oxygen-induced Platinum Nanoparticle Ripening Studied by In Situ TEM. *J. Am. Chem. Soc.* **2010,** *132*, 7968-7975.

(5) van den Berg, R.; Parmentier, T. E.; Elkjær, C. F.; Gommes, C. J.; Sehested, J.; Helveg, S.; de Jongh, P. E.; de Jong, K. P., Support Functionalization To Retard Ostwald Ripening in Copper Methanol Synthesis Catalysts. *ACS Catal.* **2015,** *5*, 4439-4448.

(6) Wettergren, K.; Schweinberger, F. F.; Deiana, D.; Ridge, C. J.; Crampton, A. S.; Rötzer, M. D.;

Hansen, T. W.; Zhdanov, V. P.; Heiz, U.; Langhammer, C., High Sintering Resistance of Size-Selected Platinum Cluster Catalysts by Suppressed Ostwald Ripening. *Nano Letters* **2014,** *14*, 5803-5809.

(7) Ouyang, R.; Liu, J.-X.; Li, W.-X., Atomistic Theory of Ostwald Ripening and Disintegration of Supported Metal Particles under Reaction Conditions. *J. Am. Chem. Soc.* **2013,** *135*, 1760-1771.

(8) Suzuki, A.; Inada, Y.; Yamaguchi, A.; Chihara, T.; Yuasa, M.; Nomura, M.; Iwasawa, Y., Time Scale and Elementary Steps of CO-Induced Disintegration of Surface Rhodium Clusters. *Angewandte Chemie International Edition* **2003,** *42*, 4795-4799.

(9) Argyle, D. M.; Bartholomew, H. C., Heterogeneous Catalyst Deactivation and Regeneration: A Review. *Catalysts* **2015,** *5*.

(10) Weststrate, C. J.; Hauman, M. M.; Moodley, D. J.; Saib, A. M.; van Steen, E.; Niemantsverdriet, J. W., Cobalt Fischer–Tropsch Catalyst Regeneration: The Crucial Role of the Kirkendall Effect for Cobalt Redispersion. *Top. Catal.* **2011,** *54*, 811.

(11) Sadasivan, S.; Bellabarba, R. M.; Tooze, R. P., Size dependent reduction-oxidation-reduction behaviour of cobalt oxide nanocrystals. *Nanoscale* **2013,** *5*, 11139-11146.

(12) Hauman, M. M.; Saib, A.; Moodley, D. J.; du Plessis, E.; Claeys, M.; van Steen, E., Re-dispersion of Cobalt on a Model Fischer-Tropsch Catalyst During Reduction-Oxidation-Reduction Cycles. *Chemcatchem* **2012,** *4*, 1411-1419.

(13) Aguinaga, A.; Montes, M., REGENERATION OF A NICKEL SILICA CATALYST POISONED BY THIOPHENE. *Applied Catalysis a-General* **1992,** *90*, 131-144.

(14) Boyes, E. D.; Gai, P. L., Environmental high resolution electron microscopy and applications to chemical science. *Ultramicroscopy* **1997,** *67*, 219-232.

(15) Alan, T.; Yokosawa, T.; Gaspar, J.; Pandraud, G.; Paul, O.; Creemer, F.; Sarro, P. M.; Zandbergen, H. W., Micro-fabricated channel with ultra-thin yet ultra-strong windows enables electron microscopy under 4-bar pressure. *Appl. Phys. Lett.* **2012,** *100*, 081903.

(16) Ring, E. A.; de Jonge, N., Microfluidic System for Transmission Electron Microscopy. *Microsc. Microanal.* **2010,** *16*, 622-629.

(17) de Jonge, N.; Bigelow, W. C.; Veith, G. M., Atmospheric Pressure Scanning Transmission Electron Microscopy. *Nano Lett.* **2010,** *10*, 1028-1031.

(18) Li, Y.; Zakharov, D.; Zhao, S.; Tappero, R.; Jung, U.; Elsen, A.; Baumann, P.; Nuzzo, R. G.; Stach, E. A.; Frenkel, A. I., Complex structural dynamics of nanocatalysts revealed in Operando conditions by correlated imaging and spectroscopy probes. **2015,** *6*, 7583.

(19) Asoro, M. A.; Ferreira, P. J.; Kovar, D., In situ transmission electron microscopy and scanning transmission electron microscopy studies of sintering of Ag and Pt nanoparticles. *Acta Mater.* **2014,** *81*, 173-183.

(20) LaGrow, A. P.; Besong, T. M. D.; AlYami, N. M.; Katsiev, K.; Anjum, D. H.; Abdelkader, A.; Costa, P. M. F. J.; Burlakov, V. M.; Goriely, A.; Bakr, O. M., Trapping shape-controlled nanoparticle nucleation and growth stages via continuous-flow chemistry. *Chem. Commun.* **2017,** *53*, 2495-2498.

(21) Benavidez, A. D.; Kovarik, L.; Genc, A.; Agrawal, N.; Larsson, E. M.; Hansen, T. W.; Karim, A. M.; Datye, A. K., Environmental Transmission Electron Microscopy Study of the Origins of Anomalous Particle Size Distributions in Supported Metal Catalysts. *ACS Catal.* **2012,** *2*, 2349-2356.

(22) Yoshida, K.; Bright, A. N.; Ward, M. R.; Lari, L.; Zhang, X.; Hiroyama, T.; Boyes, E. D.; Gai, P. L., Dynamic wet-ETEM observation of Pt/C electrode catalysts in a moisturized cathode atmosphere. *Nanotechnology* **2014,** *25*.

(23) Challa, S. R.; Delariva, A. T.; Hansen, T. W.; Helveg, S.; Sehested, J.; Hansen, P. L.; Garzon, F.; Datye, A. K., Relating Rates of Catalyst Sintering to the Disappearance of Individual Nanoparticles during Ostwald Ripening. *J. Am. Chem. Soc.* **2011,** *133*, 20672-20675.

(24) Gai, P. L.; Lari, L.; Ward, M. R.; Boyes, E. D., Visualisation of single atom dynamics and their role in nanocatalysts under controlled reaction environments. *Chemical Physics Letters* **2014,** *592*, 355-359.

(25) Hansen, P. L.; Wagner, J. B.; Helveg, S.; Rostrup-Nielsen, J. R.; Clausen, B. S.; Topsøe, H., Atom-Resolved Imaging of Dynamic Shape Changes in Supported Copper Nanocrystals. *Science* **2002,** *295*, 2053.

(26) Uchiyama, T.; Yoshida, H.; Kuwauchi, Y.; Ichikawa, S.; Shimada, S.; Haruta, M.; Takeda, S., Systematic Morphology Changes of Gold Nanoparticles Supported on CeO2 during CO Oxidation. *Angew. Chem. Int. Ed.* **2011,** *50*, 10157-10160.

(27) LaGrow, A. P.; Ward, M. R.; Lloyd, D. C.; Gai, P. L.; Boyes, E. D., Visualizing the Cu/Cu2O Interface Transition in Nanoparticles with Environmental Scanning Transmission Electron Microscopy. *J. Am. Chem. Soc.* **2017,** *139*, 179-185.

(28) LaGrow, A. P.; Ingham, B.; Cheong, S.; Williams, G. V. M.; Dotzler, C.; Toney, M. F.; Jefferson, D. A.; Corbos, E. C.; Bishop, P. T.; Cookson, J.; Tilley, R. D., Synthesis, Alignment, and Magnetic Properties of Monodisperse Nickel Nanocubes. *J. Am. Chem. Soc.* **2011,** *134*, 855-858.

(29) LaGrow, A. P.; Cheong, S.; Watt, J.; Ingham, B.; Toney, M. F.; Jefferson, D. A.; Tilley, R. D., Can Polymorphism be Used to form Branched Metal Nanostructures? *Adv. Mater.* **2013,** *25*, 1552-1556.

(30) Johnston-Peck, A. C.; Wang, J.; Tracy, J. B., Synthesis and Structural and Magnetic Characterization of Ni(Core)/NiO(Shell) Nanoparticles. *ACS Nano* **2009,** *3*, 1077-1084.

(31) Lagrow, A. P.; Alyami, N. M.; Lloyd, D. C.; Bakr, O. M.; Boyes, E. D.; Gai, P. L., In situ oxidation and reduction of triangular nickel nanoplates via environmental transmission electron microscopy. *Journal of Microscopy* **2017**, n/a-n/a.

(32) Chenna, S.; Crozier, P. A., In situ environmental transmission electron microscopy to determine transformation pathways in supported Ni nanoparticles. *Micron* **2012,** *43*, 1188-1194.

(33) Medford, J. A.; Johnston-Peck, A. C.; Tracy, J. B., Nanostructural transformations during the reduction of hollow and porous nickel oxide nanoparticles. *Nanoscale* **2013,** *5*, 155-159.

(34) Railsback, J. G.; Johnston-Peck, A. C.; Wang, J.; Tracy, J. B., Size-Dependent Nanoscale Kirkendall Effect During the Oxidation of Nickel Nanoparticles. *ACS Nano* **2010,** *4*, 1913-1920.

(35) Boyes, E. D.; Ward, M. R.; Lari, L.; Gai, P. L., ESTEM imaging of single atoms under controlled temperature and gas environment conditions in catalyst reaction studies. *Annalen Der Physik* **2013,** *525*, 423-429.

(36) Boyes, E. D.; Gai, P. L., Visualising reacting single atoms under controlled conditions: Advances in atomic resolution in situ Environmental (Scanning) Transmission Electron Microscopy (E(S)TEM). *Comptes Rendus Physique* **2014,** *15*, 200-213.

(37) Wang, C.-M.; Genc, A.; Cheng, H.; Pullan, L.; Baer, D. R.; Bruemmer, S. M., In-Situ TEM visualization of vacancy injection and chemical partition during oxidation of Ni-Cr nanoparticles. *Scientific Reports* **2014,** *4*, 3683.

(38) Wang, C.-M.; Schreiber, D. K.; Olszta, M. J.; Baer, D. R.; Bruemmer, S. M., Direct in Situ TEM Observation of Modification of Oxidation by the Injected Vacancies for Ni–4Al Alloy Using a Microfabricated Nanopost. *ACS Applied Materials & Interfaces* **2015,** *7*, 17272-17277.

(39) LaGrow, A. P.; Sinatra, L.; Elshewy, A.; Huang, K.-W.; Katsiev, K.; Kirmani, A. R.; Amassian, A.; Anjum, D. H.; Bakr, O. M., Synthesis of Copper Hydroxide Branched Nanocages and Their Transformation to Copper Oxide. *J. Phys. Chem. C* **2014,** *118*, 19374-19379.

(40) Jeangros, Q.; Faes, A.; Wagner, J. B.; Hansen, T. W.; Aschauer, U.; Van herle, J.; Hessler-Wyser, A.; Dunin-Borkowski, R. E., In situ redox cycle of a nickel-YSZ fuel cell anode in an environmental transmission electron microscope. *Acta Mater.* **2010,** *58*, 4578-4589.

(41) Richardson, J. T.; Scates, R.; Twigg, M. V., X-ray diffraction study of nickel oxide reduction by hydrogen. *Applied Catalysis A: General* **2003,** *246*, 137-150.

(42) Benton, A. F.; Emmett, P. H., The reduction of nickelous and ferric oxides by hydrogen. *J. Am. Chem. Soc.* **1924,** *46*, 2728-2737.

(43) Taylor, G. B.; Starkweather, H. W., Reduction of metal oxides by hydrogen. *J. Am. Chem. Soc.* **1930,** *52*, 2314-2325.

(44) Rodriguez, J. A.; Hanson, J. C.; Frenkel, A. I.; Kim, J. Y.; Pérez, M., Experimental and

Theoretical Studies on the Reaction of H2 with NiO: Role of O Vacancies and Mechanism for Oxide Reduction. *J. Am. Chem. Soc.* **2002,** *124,* 346-354.
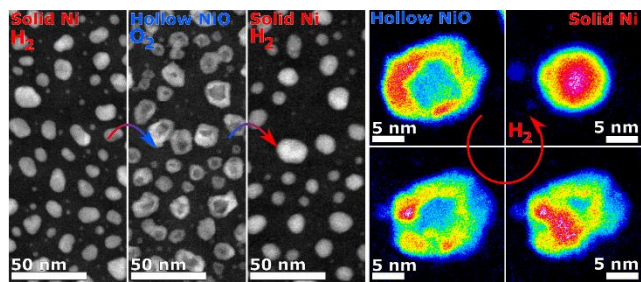
Insert Table of Contents artwork here